Research article

Marie S. Rider* and Vincenzo Giannini

Proposal for THz lasing from a topological quantum dot

https://doi.org/10.1515/nanoph-2021-0292
Received June 10, 2021; accepted August 20, 2021;
published online September 8, 2021

Abstract: Topological quantum dots (TQDs) are 3D topological insulator (TI) nanoparticles, displaying symmetry-protected surface states with discretized energies. We present a theoretical proposal to harness these energy levels in a closed lasing scheme operating in the terahertz (THz) frequency range. In this scheme, a single TQD lases from its topological surface states in the THz regime when pumped with low intensity, incoherent THz frequency light. The time scales associated with the system are unusually slow, and we find that lasing occurs with a very low threshold. THz lasers are often bulky or require intricately engineered nanostructures. Topological quantum dots present a new, compact and simple platform for THz lasing. The lasing threshold is so low, we predict that the room-temperature blackbody radiation can substantially contribute to population inversion, providing a route to room-temperature THz lasing pumped via blackbody radiation.

Keywords: nano-lasers; nanoparticles; quantum dots; THz lasers; topological insulators; topological nanophotonics.

1 Introduction

The creation of robust, low threshold sources in the terahertz (THz) gap (∼0.1–10 THz) is an important frontier in modern applied physics and this rapidly expanding field has recently received much attention. With much needed applications in bio-medicine [1], wireless communications [2] and security technologies [3], THz waves penetrate materials opaque to other wavelengths, while posing only minimal risks due to their non-ionizing behaviour (unlike for example, X-rays). Academic applications range from molecular spectroscopy [4] to sub-millimetre astronomy [5], influencing physics on vast length scales. Commercial THz lasers are still bulky and expensive to produce, and so research efforts into finding elegant, compact and inexpensive solutions are imperative.

Multiple platforms are being investigated, such as solid-state and molecular systems [6–12], metasurfaces [13], quantum gases [14] and air plasma [15]. The current state-of-the-art THz lasing system is the quantum cascade laser, which presents a compact system that can operate up to 250 K, but requires carefully designed and engineered nanostructures, and current injection [12].

A separate focus of study is the use of topological systems as a robust lasing platform, which is developing as an exciting field. Topological systems have had most success in the mid-infrared [16–26], although work has been done on THz lasers using 2D topological insulator quantum dots (TIQDs), requiring electron injection and an IR pump [27].

Topological quantum dots (TQDs) are 3D topological insulator nanoparticles with radius $\leq$ 100 nm, whose topological surface states undergo quantum confinement resulting in a discretised Dirac cone, with energy levels which increase in degeneracy away from the Dirac point. The pioneering works on TI quantum dots have studied the properties of circular TI disks and non-equiaxial 3D TI systems with cylindrical confinement [28–31], with potential applications in memory storage [32], spin field-effect transistors [33] and other spintronic devices [34]. 2D TI QDs have been proposed for THz lasing previously [27] utilising electron injection and an IR pump. The current work focuses on equiaxial 3D TI nanoparticles, which is a small but steadily expanding field [35–42]. Much like other types of quantum dots and atomic systems, the discrete energy levels of the TQD make it a natural system for controlled interactions with light. TQDs have energy levels separated

***Corresponding author**: **Marie S. Rider**, The Blackett Laboratory, Imperial College London, SW7 2AZ, London, UK,
E-mail: marie.rider@ic.ac.uk. https://orcid.org/0000-0001-5130-1901
Vincenzo Giannini , Instituto de Estructura de la Materia (IEM-CSIC), Consejo Superior de Investigaciones Científicas, Serrano 121, 28006 Madrid, Spain; Technology Innovation Institute, Building B04C, Abu Dhabi P.O. Box 9639, United Arab Emirates; and Centre of Excellence ENSEMBLE3 sp. z o.o., Wolczynska 133, Warsaw, 01-919, Poland, Homepage: www.GianniniLab.com, E-mail: v.giannini@csic.es

by THz frequencies, making them a potential route to THz lasing.

In this work we use Monte Carlo (MC) simulations to demonstrate that for a model system of a single TQD in an open cavity at zero temperature, the TQD states can be pumped and act as an active gain medium, emitting coherent light in the THz. We show that lasing from a single TQD is possible with very low threshold. One of the major technological distinctions between the TQD laser and other THz lasers (such as molecular THz lasers and TIQD lasers) is that we do not pump between bulk bands, but instead we use transitions within the Dirac cone to both pump and lase. This is possible due to the energy level configuration and selection rules of the TQD [38, 40]. An important consequence of THz pumping is that the density of thermal, room temperature photons at this frequency (as opposed to those present at optical and IR frequencies) is high enough to substantially contribute to population inversion in the lasing transition, such that the need for an external pumping source beyond blackbody radiation would be greatly reduced. The closed system of states near the Dirac point used in the lasing scheme conserves electron number, meaning that electron injection is not needed to sustain lasing. These features, alongside the unusual time scales in the system and the robustness of the TQD states make for a novel but very simple implementation. Experimental progress in producing TI nanostructures such as nanowires [43–47] and finite thickness nanodisks and nanoplates [48–53] has been very successful, and there has been recent progress with equiaxial 3D TI nanoparticles [36]. The concepts used to demonstrate THz lasing in this work with equiaxial 3D TI nanoparticles, using a THz pump and no current injection, could be straightforwardly extended to TI nanostructures of differing dimensions. As well as adding another tool to the tool-box of THz lasing, TQDs could also find use in other technological applications, such as quantum memory and quantum computing [40], and as components of hybrid systems, such as coupled to semiconductor quantum dots [41] and quantum emitters [42].

This paper is structured as follows: in Section 2 we will briefly review the theory of spherical topological insulator nanoparticles and in Section 3 we discuss their optical properties. In Section 4 we will describe how higher order corrections to the Dirac cone become important when a TI nanoparticle is placed in a high quality cavity, and how this can be utilised to create a closed scheme of energy levels. We will then describe in Section 5 how Monte Carlo simulations are used to capture the dynamics of the system when pumped and in Section 6 give results demonstrating that a single TI nanoparticle can be used as a THz laser at zero temperature. We discuss how the low threshold of this system could allow for room temperature thermal photons to contribute to the pumping source, and conclude in Section 7 with an outlook.

2 3D topological insulator quantum dots

Topological insulator (TI) nanostructures support symmetry-protected surface states with quantised energy levels. The model Hamiltonian describing topological insulator materials is given by

$$\begin{aligned}\mathbf{H}(\mathbf{k}) = m(\mathbf{k})\mathbb{1}_2 \otimes \boldsymbol{\sigma_3} + Ak_z\boldsymbol{\sigma_3} \otimes \boldsymbol{\sigma_1} \\ + Ak_x\boldsymbol{\sigma_1} \otimes \boldsymbol{\sigma_1} + Ak_y\boldsymbol{\sigma_2} \otimes \boldsymbol{\sigma_1},\end{aligned} \tag{1}$$

where $m(\mathbf{k}) = m_0 + m_1|\mathbf{k}|^2$, with parameters calculated via *ab initio* calculations [54]. A relates to the strength of spin–orbit coupling (SOC) in the material, averaged over the three Cartesian axes. This approximation of isotropic SOC allows for the analytical description of the topological surface states and their energy levels. From this bulk Hamiltonian both an effective surface Hamiltonian (which takes the form of a Dirac Hamiltonian) and the surface states can be derived (discussed in more detail in Supplementary Material S1). For spherical nanoparticles of radius $5 \leq R/\text{nm} \leq 100$ [37–40] (presented schematically in Figure 1A), close to the Γ-point the wavefunctions for these surface states are given by

$$\begin{aligned}\Psi_{s,n,m}(\xi,\varphi) &= \langle \xi,\varphi|\Psi_{s,n,m}\rangle \\ &= \frac{e^{im\varphi}}{2\sqrt{\pi}R} N_{n,m}\chi_{s,n,m}(\xi),\end{aligned} \tag{2}$$

where

$$\chi_{s,n,m}(\xi) = \begin{pmatrix} (1-\xi)^{\frac{1}{2}\sigma^-}(1+\xi)^{\frac{1}{2}\sigma^+} J_n^{\sigma^-\sigma^+}(\xi) \\ -\dfrac{sm}{|m|}(1-\xi)^{\frac{1}{2}\sigma^+}(1+\xi)^{\frac{1}{2}\sigma^-} J_n^{\sigma^+\sigma^-}(\xi) \end{pmatrix}, \tag{3}$$

and $\sigma^{\pm} = |m \pm \frac{1}{2}|$, $\xi = \cos\vartheta$, $s = \pm$, $n = 0, 1, 2, \ldots$, $m = \pm 1/2, 3/2, 5/2, \ldots$ and $J_n^{\sigma^{\pm}\sigma^{\mp}}$ are Jacobi polynomials [39]. $N_{n,m}$ is a normalisation factor (given in Supplementary Material S2). The corresponding discretized energy levels of these states are given by

$$E_{s,n,m} = \frac{sA}{R}\left(n + |m| + \frac{1}{2}\right). \tag{4}$$

Close to the Γ-point the energy levels are linearly spaced, and increase in degeneracy away from the Dirac point (i.e. 2, 4, 6, 8, …) as illustrated in Figure 1B. The energy values are inversely proportional to R, and for large R we

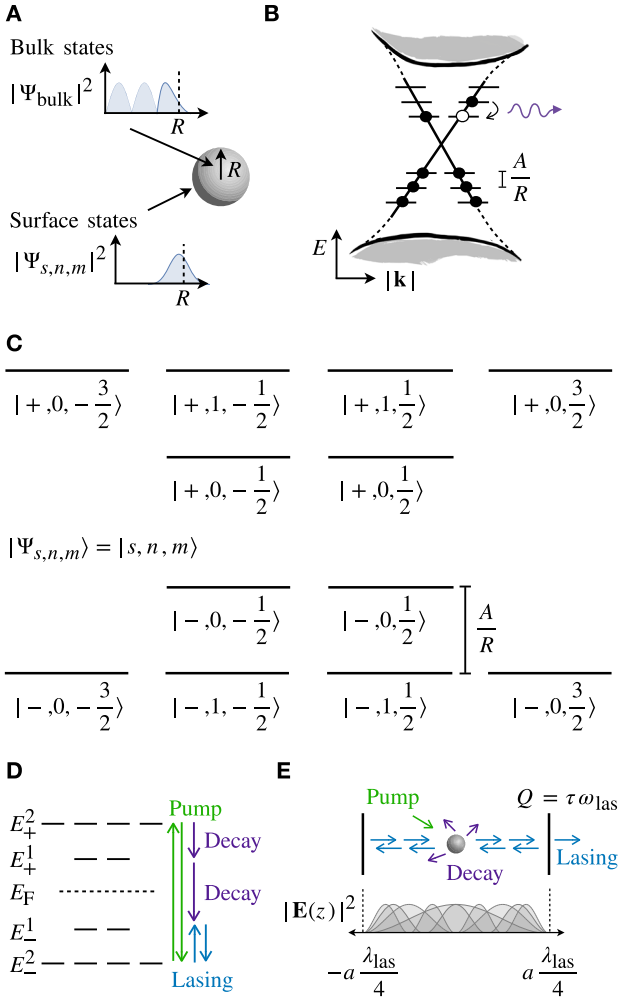

Figure 1: Lasing topological quantum dots: (A) schematic of topological quantum dot, showing bulk and surface states. (B) Discretization of Dirac cone for small nanoparticles, with energy level separation near the Dirac point inversely proportional to particle radius, R and directly proportional to material-dependent constant A. Transitions between energy levels are facilitated by the absorption or emission of THz light. (C) The discrete energy levels are labelled by three quantum numbers $|s,n,m\rangle$. We present the labels for the four energy levels closest to the Dirac point. (D) Example lasing scheme with interband pumping and bottom-most transition as the lasing transition. Fermi level $E_F = 0$. (E) Schematic of TQD in cavity of length $a\lambda_{las}/2$ with a an integer, lasing frequency ν_{las}, quality factor $Q = \tau\omega_{las}$ with τ the cavity lifetime. The c-axis of the material is aligned with the cavity axis. Spatial dependence of the cavity electric field gives spatial dependence of photonic DOS and consequently transition rates. TQD placed at centre of cavity for maximal interaction with the cavity field, meaning that only modes with a odd will have non-zero transition rates in the cavity axis.

recover the expected continuum Dirac cone. Examples of the energy levels associated with quantum numbers (s,n,m) are given in Figure 1C. The system of discrete energy levels can be tuned with particle size (much like the energy levels of a semiconductor quantum dot or TIQD), encouraging us to refer to this system as a topological quantum dot (TQD). The key differences between TQDs and semiconductor quantum dots are (i) the delocalization of states for TQDs versus the relatively localized states of the semiconductor counterpart, (ii) the quantisation of surface states rather than bulk states, which in turn affects (iii) the frequency-range of operation, which for semiconductor quantum dots is usually in the visible range and near infrared, but for TQDs is in the THz, e.g. for a Bi_2Se_3 TQD of $5 < R/\text{nm} < 100$, $A = 3.0$ eV Å [54] and the spacing between two energy levels is 0.72–14.4 THz, contrasting with a band gap of 220 meV ∼ 53.2 THz.

The high tunability of this system, combined with the unusual degeneracy and spacing of the energy levels suggests an interesting nanophotonic system [35–37]. The goal of this paper will be to demonstrate that by pumping the electrons of the surface states between discrete energy levels while placed in a cavity (described schematically in Figures 1D and E), we can use a TQD as a THz laser. With this in mind, we will now discuss the TQD optical properties.

3 Optical properties of TQDs

For a TQD with material c-axis aligned along the z-axis, the electric dipole (E1) selection rules for allowed optical transitions between TQD energy levels such that $|\Psi_i\rangle \to |\Psi_f\rangle$, where $i = (s,n,m)$ and $f = (s',n',m')$ can be found by examining the E1 matrix element (with some explicit examples given in Supplementary Material S3),

$$V_{i,f}(\omega_{i,f}) = \langle\Psi_f|\mathbf{r}\cdot\epsilon|\Psi_i\rangle, \tag{5}$$

where ϵ is the polarisation vector of the incoming light. For stimulated processes, the selection rules for incoming right-hand (RH) polarised light along the z-axis are given by

$$\Delta s = 0, \quad \Delta(n+|m|) = \pm 1, \quad \Delta m = 1, \tag{6}$$

$$\Delta s \neq 0, \quad \Delta(n+|m|) = 0, \quad \Delta m = 1. \tag{7}$$

For incoming left-hand (LH) polarised light along the z-axis, the selection rules are

$$\Delta s = 0, \quad \Delta(n+|m|) = \pm 1, \quad \Delta m = -1, \tag{8}$$

$$\Delta s \neq 0, \quad \Delta(n+|m|) = 0, \quad \Delta m = -1. \tag{9}$$

Figure 2 illustrates the allowed stimulated transitions for a surface state with energy $E_{s,n,m} = -2A/R$ when excited with either LH or RH polarized light. Note that there are two distinct types of transitions: (i) interband transitions which

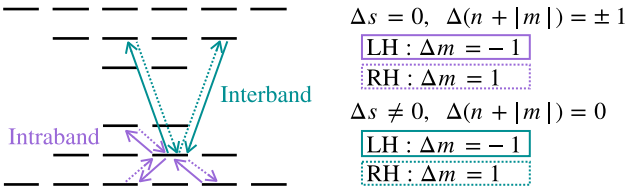

Figure 2: TQD selection rules: E1 selection rules for TQD state $|-,\ 1,\ 1/2\rangle$. Interband (green) transitions couple energy levels above and below the Dirac point. Intraband (purple) transitions couple levels within the same section of the Dirac cone. Both left-hand (solid arrows) and right-hand (dotted arrows) polarised light facilitate transitions.

couple the upper and lower halves of the Dirac cone requiring energy $\Delta E = 2E_{s,n,m}$ (green arrows), and (ii) intraband transitions which couple nearest energy levels, requiring $\Delta E = A/R$ (purple arrows). The transition rates of allowed stimulated E1 transitions are given by

$$\Gamma_{\mathrm{i}\to\mathrm{f}}^{\mathrm{stim}} = 2\pi^2\alpha\frac{c}{\hbar}\bar{u}(\omega_{\mathrm{i,f}})|V_{\mathrm{i,f}}|^2, \tag{10}$$

where $\bar{u}(\omega_{\mathrm{i,f}}) = \hbar\omega_{\mathrm{i,f}}\bar{n}(\omega_{\mathrm{i,f}})\rho(\omega_{\mathrm{i,f}})$, is the energy density at frequency $\omega_{\mathrm{i,f}} = 2\pi\nu_{\mathrm{i,f}}$ and $\bar{n}(\omega_{\mathrm{i,f}})$ is the average number of photons in mode $\omega_{\mathrm{i,f}}$. We have assumed symmetry in photon polarisation such that $n_{\mathrm{LH}}(\omega_{\mathrm{i,f}}) = n_{\mathrm{RH}}(\omega_{\mathrm{i,f}}) = \bar{n}(\omega_{\mathrm{i,f}})/2$. $V_{\mathrm{i,f}}$ is the matrix element given in Eq. (5). The density of states in free space is $\rho_{\mathrm{free}}(\omega_{\mathrm{i,f}}) = \omega_{\mathrm{i,f}}^2/\pi^2c^3$, and at the centre of an open cavity of quality factor Q, formed of two parallel mirrors separated by a distance L, with incoming light oriented along the cavity axis,

$$\rho_{\mathrm{cav}}(\omega_{\mathrm{i,f}}) = \frac{2}{\pi L}\frac{Q\omega_{\mathrm{cav}}}{\omega_{\mathrm{cav}}^2 + 4Q^2(\omega_{\mathrm{i,f}} - \omega_{\mathrm{cav}})^2}. \tag{11}$$

The rate of spontaneous emission is given in free space by

$$\Gamma_{\mathrm{i}\to\mathrm{f}}^{\mathrm{spon}} = \frac{4\alpha\omega_{\mathrm{f,i}}^3}{3c^2}|\langle\Psi_{\mathrm{f}}|\mathbf{r}|\Psi_{\mathrm{i}}\rangle|^2, \tag{12}$$

and in the open cavity by

$$\Gamma_{\mathrm{i}\to\mathrm{f}}^{\mathrm{spon}} = \frac{8\pi\alpha c}{L}\frac{Q\omega_{\mathrm{i,f}}\omega_{\mathrm{cav}}}{\omega_{\mathrm{cav}}^2 + 4Q^2(\omega_{\mathrm{i,f}} - \omega_{\mathrm{cav}})^2}|\langle\Psi_{\mathrm{f}}|\mathbf{r}|\Psi_{\mathrm{i}}\rangle|^2. \tag{13}$$

Equations (12) and (13) are polarisation independent. For a Bi_2Se_3 nanoparticle of radius $R = 50$ nm in the linear approximation, the smallest frequency coupling states within the quantised Dirac cone is $\nu = 1.44$ THz and the spontaneous emission rate in free space for the intraband transition between levels $|+,\ 1,\ -1/2\rangle$ and $|+,\ 0,\ 1/2\rangle$ is 7.0×10^3 s^{-1}. Interband transitions are typically much faster, with the spontaneous transition in free space from $|+,\ 1,\ -1/2\rangle$ to $|-,\ 1,\ 1/2\rangle$ given by 1.4×10^5 s^{-1}, with transition frequency 5.76 THz. These rates are much slower than comparable processes in semiconductor quantum dots, whose spontaneous emission rates are typically in the range 10^6–10^9 s^{-1} depending on their structure [55, 56]. This is due to the frequency dependence of the transition rates, with typical energy level separation in semiconductor quantum dots much greater than in TQDs.

4 Higher order corrections

Close to the Γ-point the surface state dispersion relation is described well by linear $\mathbf{k}\cdot\mathbf{p}$ theory and taken to be linear, and so the energy levels of the TQD surface states can be considered equally spaced. When higher order terms are to be taken into account, we return to the continuum model and use the dispersion relation

$$E_{\mathrm{c,v}} = \pm A|\mathbf{k}| + A_1|\mathbf{k}|^2, \tag{14}$$

where $E_{\mathrm{c,v}}$ give the energies of the conduction and valence bands, respectively. For Bi_2Se_3, $A = 3.0$ eV Å, $A_1 = 22.2$ eV Å^2, and for Bi_2Te_3, $A = 2.0$ eV Å, $A_1 = 35.3$ eV Å^2 [54]. More details on these values are given in Supplementary Material S1. On confinement of the surface states, $|\mathbf{k}| \sim 1/R$ and so the correction is proportional to $1/R^2$, demonstrated in Figure 3A. For a Bi_2Se_3 TQD of $R = 50$ nm, without the correction all nearest-level transitions occur with frequency $\nu^{(0)} = 1.44$ THz (asides from the transition coupling levels directly above and below the Γ-point, which couples at frequency $2\nu^{(0)}$), as illustrated in Figure 3B. When taking the correction into account, transition frequencies in both the valence and conduction bands rapidly become off-resonant with the first transition in each band. The first and second transition frequencies in the upper Dirac cone show a disparity of 3%. The first and third transition frequencies differ by 6%, as shown in Figure 3B. The first transition frequencies in the valence and conduction bands differ by ∼ 9%. Variation in frequency is more rapid in smaller particles, and in materials for which A_1 is large. This disparity can thus be increased by considering a TQD of smaller radius, or by using a different material such as Bi_2Te_3. It should be noted that interband transitions are unaffected due to the cancellation of the second-order correction.

When placed in a cavity, higher-order corrections to the TQD Hamiltonian must clearly be considered as transitions between energy levels will rapidly become off-resonant with the cavity frequency if tuned to a single transition frequency. For a cavity with lifetime greater than the timescale of free space spontaneous emission due to

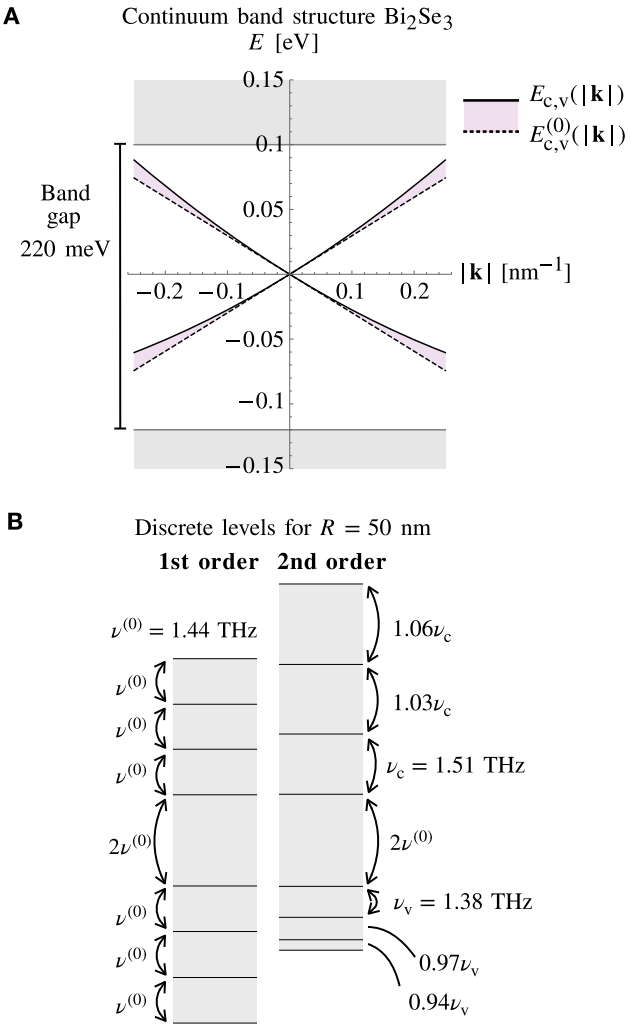

Figure 3: k.p breakdown: (A) continuum band structure for Bi_2Se_3 with Dirac cone in the band gap (=220 meV [61]). Band structure up to and including k^2 terms (solid black line), $E_{c,v}(|\mathbf{k}|)$ (for the conduction and valence band sections of the Dirac cone, respectively), deviates from the linear $\mathbf{k}\cdot\mathbf{p}$ approximation (dotted black line), $E^{(0)}_{c,v}(|\mathbf{k}|)$. The disparity increases away from the Gamma point. (B) For a $R = 50$ nm nanoparticle, discretised energy levels are expected. In the linear approximation, transition frequency $\nu^{(0)} = 1.44$ THz, whereas when taking into account the k^2 term, sequential transitions away from the Γ-point deviate increasingly.

intraband transitions, $Q = \tau\omega_{las} > \tau_{spon}\omega_{las}$, $\tau_{spon} \approx 10^{-4}$ s for a $R = 50$ nm particle, so $Q > 10^8$. This exceedingly high Q factor is due to the unusual combination of a high transition frequency and long timescale. It is clear that for a cavity of such high Q factor, the line-width is much smaller than the energy level separation, and the only mode coupled to the cavity will be the single resonant transition, such that $\rho_{cav}(\omega) = 2Q/\pi\omega_{i,f}L$. All other transitions within the Dirac cone and in the direction of the cavity axis will be drastically suppressed and considered negligible. However, for an open cavity these transitions may still occur in all directions not directly parallel to the cavity axis.

5 Surface state dynamics using Monte Carlo (MC)

We now explain how a Monte Carlo method is used to study the time-evolving surface state dynamics of a TQD interacting with the electromagnetic field in a cavity.

We move to a Fock basis, in which the quantum state of the TQD can be described by

$$|\Psi\rangle = \prod_{\alpha=1}^{2M} \otimes |N_\alpha\rangle, \tag{15}$$

where we take a product state of the M states above and below the Dirac point, with $2M$ states in total forming a closed system of energy levels. Each state $\alpha = (s, n, m)$ obeys fermionic occupation rules such that $N_\alpha = 0$ or 1. The photon density for the pump $\bar{n}_{pump}$ is kept constant, and the photon densities for modes not resonant with the cavity are zero. Stimulated emission will only be triggered by photons in the cavity axis and thus coherent with the lasing mode, ν_{las}, which is defined by the first spontaneous emission of frequency ν_{las}. The cavity (with quality factor Q) enforces feedback of coherent ν_{las} photons.

For a given time step dt, the transition rates given in Eqs. (10), (12) and (13) are converted to probabilities $p_{i,f} = \Gamma_{i\to f}\mathrm{d}t \ll 1$, where for stimulated processes $\Gamma_{i\to f}$ will dynamically change as $\bar{n}_{i,f}$ evolves via the dynamics. The TQD couples to the cavity mode with a rate proportional to the spatially-dependent probability density of the standing wave cavity mode shown in Figure 1E. For positive feedback of lasing frequency ν_{las}, we use a cavity of length $L = a\lambda_{las}/2$, with a an integer. For simplicity, we consider a TQD at the centre of the cavity, such that the spatial-dependence of the electric field is maximal for odd multiples of the fundamental cavity mode, ν_{las}, and zero for even multiples.

The initial conditions are set by occupying states up to the desired Fermi level E_F. For a given time step, all electrons may transition between states with the probabilities calculated from the relations given. At the end of the time step, it is checked that the transitions have obeyed fermionic occupation rules (such that there is maximum one electron in any given state). If the transitions have resulted in multiple occupancy of any state, the time step is reset and the system required to undertake the step again.

When a physically allowed time step has been undertaken, the entire system updates and progresses to the next time step. In this way, the system evolves whilst observing fermionic occupation rules. A single evolution of the system gives a single quantum trajectory, while averaging the simulation over many iterations gives the average expected results of a single TQD, or if multiplied by N, gives the result of N uncorrelated TQDs [57].

6 THz lasing from a single TQD

We now describe a specific closed lasing scheme using discrete surface states of the TQD at $T = 0$. We start with a single Bi_2Se_3 TQD in a Fabry–Pérot cavity with the material c-axis aligned with the cavity axis and Fermi level at $E_F = 0$. The TQD is pumped using an interband transition, and the cavity is tuned to the lowest intraband transition in the scheme, as illustrated in Figure 1D. The arguments in Section 4 show that all other transitions will be suppressed in the cavity axis.

We pump the system with photons of energy $E_+^2 - E_-^2$, away from the cavity axis as shown in Figure 1D and tune the cavity to the transition $\nu_{las} = (E_-^1 - E_-^2)/h$ by using an open Fabry–Pérot cavity of length $L = a\lambda_{las}/2$. For a $R = 50$ nm particle, this requires pumping with photons of frequency 5.76 THz and the lasing frequency will be 1.38 THz. We choose a cavity length $L = 100.5\lambda_{las} \approx 2.2$ cm. All processes not directly in the cavity axis will occur with the rate given in Eq. (12), while in the cavity the stimulated rates will be given by Eq. (10) with the density of states

$$\rho(\omega_{i,j}) = \frac{Q}{2\pi L\omega_{i,f}}\delta\left(\omega_{i,j} - 2\pi\nu_{las}\right), \tag{16}$$

and the spontaneous rates in the cavity by Eq. (13). We place the TQD in the centre of the cavity at the peak of electric field density as displayed in Figure 1E. All transitions in frequencies other than ν_{las} are suppressed in the cavity axis. Only four energy levels are considered in the simulation as all other levels are decoupled, and all processes involved are depicted in Figure 4A, with bold arrows indicating stimulated processes and dotted arrows indicating spontaneous processes. For fixed $Q \sim 10^9$, the dynamics of the system are tuned only with the pumping rate, which in turn is controlled by $\bar{n}_{pump} = \bar{n}\left(\omega_{pump}\right)$ of the pumping light. For $\bar{n}_{pump} = 1$, the evolution of the normalised occupation of energy levels, $\bar{N}/N_{max}$, is given in Figure 4B. Steady state is quickly achieved, with clear population inversion between levels E_-^2 and E_-^1. Gain for the lasing transition is given by

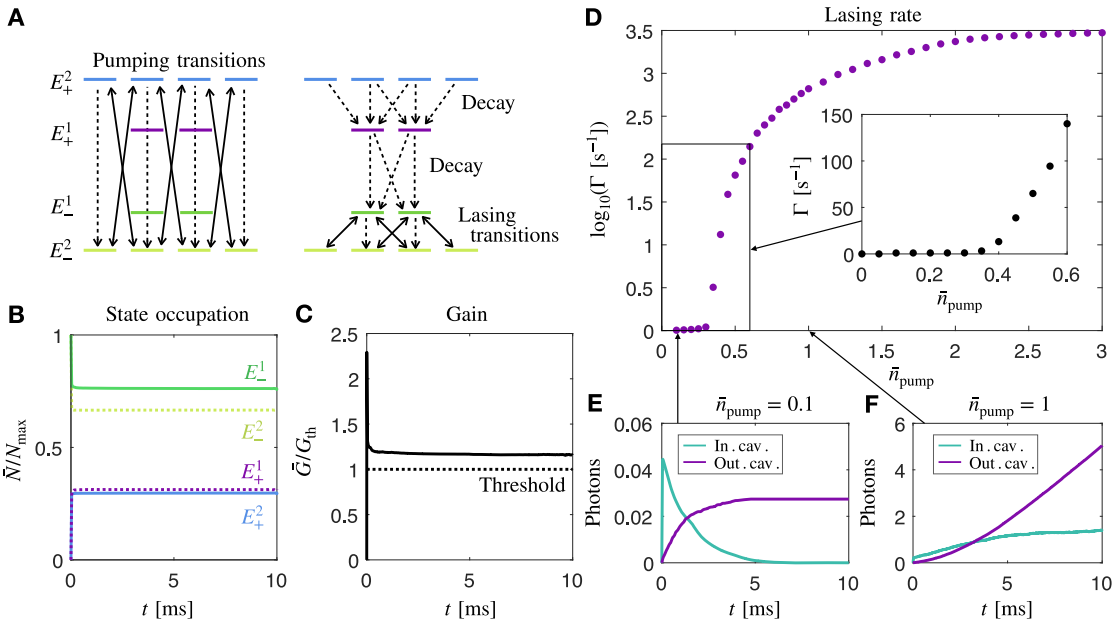

Figure 4: TQD lasing: (A) schematic of all lasing scheme transitions. Solid lines denote stimulated processes (and downwards spontaneous processes) and dashed lines denote spontaneous processes only. (B) Evolution of normalised state occupation for $E_F = 0$, $\bar{n}_{pump} = 1$. Population inversion between energy levels E_-^1 and E_-^2 is demonstrated and (C) gain above threshold for this transition is demonstrated. (D) Steady-state lasing rate (coherent photons emitted from cavity per second) for varying $\bar{n}_{pump}$ with inset showing low pumping regime $0 \leq \bar{n}_{pump} \leq 0.6$, with a lasing threshold of ~ 0.35. (E) shows the number of coherent photons inside the cavity and emitted from the cavity as a function of t for $\bar{n}_{pump} = 0.1$, which is below the lasing threshold and (F) $\bar{n}_{pump} = 1$ which is above the lasing threshold.

$$\bar{G} = \sum_{i<j} \sigma_{j\to i} \left(\bar{N}_j - \bar{N}_i\right) \delta(\omega_{i,j} - 2\pi\nu_{las}), \tag{17}$$

where $\sigma_{j\to i} = \Gamma_{j\to i}/c\bar{n}_{i,j}$ is the transition cross-section and $\bar{N}_i$ is the average occupation of surface state i. $\bar{G}$ for $\bar{n}_{pump} = 1$ is plotted in Figure 4C. A maximum is achieved nearly instantaneously as electrons are excited from states with energy E_-^2 to E_+^2, creating population inversion in the lasing transition. Steady state is quickly achieved, with gain above the threshold value. Threshold gain is given by $G_{th} = 1/\tau_{las}c$, as internal losses are taken to be negligible in this simulation.

Displayed in Figure 4D is the dependence of the lasing rate with varying $\bar{n}_{pump}$. Lasing is found to occur for $\bar{n}_{pump} \geq 0.35$ (see inset of Figure 4D). Below threshold, such as for $\bar{n}_{pump} = 0.1$ as demonstrated in Figure 4E, coherent photons in the cavity (teal line) do not build up rapidly enough to compensate for photons being absorbed by the TQD or emitted from the cavity and so the number of cavity photons decays to 0. Lasing does not occur. Above threshold, such as for $\bar{n}_{pump} = 1$ displayed in Figure 4F, a critical number of coherent photons build up in the cavity such that lasing can occur. The number of coherent photons in the cavity (teal line) slowly increases from 0 until a steady state is achieved. Coherent photons are emitted from the cavity (purple line) at a constant rate. The slope of this line gives the photon emission rate, $\Gamma \sim 6.6 \times 10^2$ s^{-1}. The power of this lasing can be calculated by assuming photons are emitted over an area commensurate with the cross-section of the nanoparticle, such that $P = \Gamma h\nu_{las}/\pi R^2 \sim 7.7 \times 10^{-5}$ W/m^2. The incoming power is approximately 1.0 W/m^2. The power conversion (power in vs power out) is roughly 0.0075% efficiency. This is very low, but it should be remembered that we are considering a single TQD. The power output and thus efficiency should increase dramatically with increased number of TQDs.

Above the threshold value of $\bar{n}_{pump}$ there is a small range in which the lasing rate exponentially increases, and then the lasing rate increases approximately linearly with increased $\bar{n}_{pump}$. Competition between processes of different time-scales in the system (cavity emission rate, spontaneous emission rate and stimulated emission rate at the cavity frequency) eventually results in slowing of the increase in the lasing rate, and a maximum lasing rate of $\sim 10^{3.5}$ s^{-1}. The lasing rates of this system have a very low threshold, but also occur at very slow time scales. This is due to the interesting interplay of length and energy scales in this system. While the lasing rates can be increased by the addition of more TQDs in the system, the system of a single TQD could offer interesting technological applications where the slow production of coherent photons is coveted.

The simulations at $T = 0$ described in this section were conducted for a $R = 50$ nm Bi_2Se_3 TQD requiring a pump with frequency 5.76 THz. At room temperature, the number of thermal photons in the pumping mode is $\bar{n}_{pump} = 0.66$, which is above the lasing threshold found for the proof-of-principle case. For $35 \leq R/\text{nm} \leq 100$, lasing frequency for the described setup is 0.70–1.93 THz, with a required pumping frequency of 2.88–8.23 THz. At room temperature, the number of photons in the pumping mode is $0.37 \leq n_{pump} \leq 1.72$, which is above threshold for all cases. For the same lasing scheme but using Bi_2Te_3, with $35 \leq R/\text{nm} \leq 100$, the lasing frequencies achieved are 0.46–1.2 THz, the pumping frequencies required are 1.94–5.54 THz, and the number of photons per mode at room temperature at the pumping frequency is in the range 0.70–2.76, which again is well above lasing threshold.

The simulations of this work were undertaken at $T = 0$ K, and as such electron–phonon interactions were not considered, due to the absence of thermal crystal vibrations at 0 K. When considering the extension to finite temperature, the potential effects of electron–phonon interactions should be discussed. At finite temperature, surface electrons in Bi_2Se_3 couple to a single optical phonon at ~ 1.9 THz [58–60]. In nanoparticles, scattering can only occur if the phonon exactly matches the energy difference between the states, due to the discrete nature of the surface states. To suppress phonon-induced non-radiative decay, it is important to choose a nanoparticle size (and thus surface state level separation) such that all transition frequencies necessary for the lasing scheme reside in the phonon gaps of the material. For the four level scheme described in this work (which can be extended to any lasing scheme of $2M$ states as described previously), this condition only negates schemes in which ν_v, ν_c, $2\nu^{(0)}$ or $4\nu^{(0)}$ equal 1.9 THz. This means avoiding particle sizes of $R = 35.5$ nm, 40 nm, 75.5 nm or 151 nm (at which size, the assumption of spatial confinement of the surface states is anyway no longer valid). Lasing effects should not be diminished by phonon interactions so long as the immediate range of frequencies around the phonon resonance are avoided.

All results presented so far have been for a single TQD. For multiple TQDs interacting via a single cavity mode (i.e. multiple TQDs aligned along the cavity axis), coherent photons emitted from one TQD will be available to trigger stimulated emission events in other TQDs. It is expected that the lasing rate will be amplified exponentially with increasing number of TQDs.

7 Outlook

By considering higher-order corrections to the surface state Hamiltonian of a TQD, we have shown that a closed lasing scheme can be created such that a single TQD will produce coherent THz frequency light. Lasing occurs at a very low threshold, but also with an unusually slow time scale. We have demonstrated that population inversion can be achieved and that lasing can occur with a very low threshold – so low in fact, that the number of photons present in blackbody radiation at room-temperature is greater than the number needed to pump the system. At room temperature, blackbody radiation will thus contribute significantly to population inversion in the lasing transition. This is only possible due to employing a THz pump. This concept deserves future investigation due to the important technological repercussions. To realistically demonstrate that lasing will occur at room temperature, we expect a 3D, closed cavity with a frequency-modulated Q factor will be required to control photon density and avoid thermal equilibrium. There is much work yet to be done to explore this system, but this scheme paves the way towards a novel, compact room-temperature THz lasing source.

Author contribution: All the authors have accepted responsibility for the entire content of this submitted manuscript and approved submission.

Research funding: M. S. R. would like to acknowledge the financial support of the Centre for Doctoral Training on Theory and Simulation of Materials at Imperial College London funded by EPSRC Grant No. EP/L015579/1. V. G. acknowledges the Spanish Ministerio de Economia y Competitividad for financial support through the grant NANOTOPO (FIS2017-91413-EXP), and also the Ministerio de Ciencia, Innovación y Universidades through the grant MELODIA (PGC2018-095777-B-C21). V. G. thanks the "ENSEMBLE3 - Centre of Excellence for nanophotonics, advanced materials and novel crystal growth-based technologies" project (GA No. MAB/2020/14) carried out within the International Research Agendas programme of the Foundation for Polish Science co-financed by the European Union under the European Regional Development Fund and the European Union's Horizon 2020 research and innovation programme Teaming for Excellence (GA. No. 857543) for support of this work.

Conflict of interest statement: The authors declare no conflicts of interest regarding this article.

References

[1] X. Yang, X. Zhao, K. Yang, et al., "Biomedical applications of terahertz spectroscopy and imaging," *Trends Biotechnol.*, vol. 34, no. 10, pp. 810–824, 2016.

[2] T. Kleine-Ostmann and T. Nagatsuma, "A review on terahertz communications research," *J. Infrared, Millim. Terahertz Waves*, vol. 32, no. 2, pp. 143–171, 2011.

[3] J. F. Federici, B. Schulkin, F. Huang, et al., "THz imaging and sensing for security applications - explosives, weapons and drugs," *Semicond. Sci. Technol.*, vol. 20, no. 7, p. S266, 2005.

[4] J. B. Baxter and G. W. Guglietta, "Terahertz spectroscopy," *Anal. Chem.*, vol. 83, no. 12, pp. 4342–4368, 2011.

[5] G. L. Pilbratt, J. R. Riedinger, T. Passvogel, et al., "Herschel Space Observatory - an ESA facility for far-infrared and submillimetre astronomy," *Astron. Astrophys.*, vol. 518, p. L1, 2010.

[6] Y. P. Gousev, I. V. Altukhov, K. A. Korolev, et al., "Widely tunable continuous-wave THz laser," *Appl. Phys. Lett.*, vol. 75, no. 6, pp. 757–759, 1999.

[7] E. D. Valle and A. Kavokin, "Terahertz lasing in a polariton system: quantum theory," *Phys. Rev. B*, vol. 83, no. 19, p. 193303, 2011.

[8] S. Kumar, C. Wang, I. Chan, Q. Hu, and J. L. Reno, "A 1.8-THz quantum cascade laser operating significantly above the temperature of $\hbar\omega k_b$," *Nat. Phys.*, vol. 7, no. 2, pp. 166–171, 2011.

[9] A. Pagies, G. Ducournau, and J.-F. Lampin, "Low-threshold terahertz molecular laser optically pumped by a quantum cascade laser," *APL Photonics*, vol. 1, no. 3, p. 031302, 2016.

[10] I. Y. Chestnov, V. A. Shahnazaryan, A. P. Alodjants, and I. A. Shelykh, "Terahertz lasing in ensemble of asymmetric quantum dots," *ACS Photonics*, vol. 4, no. 11, pp. 2726–2737, 2017.

[11] Y. Zeng, B. Qiang, and Q. J. Wang, "Photonic engineering technology for the development of terahertz quantum cascade lasers," *Adv. Opt. Mater.*, vol. 8, no. 3, p. 1900573, 2020.

[12] A. Khalatpour, A. K. Paulsen, C. Deimert, Z. R. Wasilewski, and Q. Hu, "High-power portable terahertz laser systems," *Nat. Photonics*, vol. 15, no. 1, pp. 16–20, 2021.

[13] S. Keren-Zur, M. Tal, S. Fleischer, D. M. Mittleman, and T. Ellenbogen, "Generation of spatiotemporally tailored terahertz wave packets by nonlinear metasurfaces," *Nat. Commun.*, vol. 10, no. 1, pp. 1–6, 2019.

[14] P. Chevalier, A. Amirzhan, F. Wang, et al., "Widely tunable compact terahertz gas lasers," *Science*, vol. 366, no. 6467, pp. 856–860, 2019.

[15] A. D. Koulouklidis, C. Gollner, V. Shumakova, et al., "Observation of extremely efficient terahertz generation from mid-infrared two-color laser filaments," *Nat. Commun.*, vol. 11, no. 1, pp. 1–8, 2020.

[16] P. St-Jean, V. Goblot, E. Galopin, et al., "Lasing in topological edge states of a one-dimensional lattice," *Nat. Photonics*, vol. 11, no. 10, pp. 651–656, 2017.

[17] B. Bahari, A. Ndao, F. Vallini, A. El Amili, Y. Fainman, and B. Kanté, "Nonreciprocal lasing in topological cavities of arbitrary geometries," *Science*, vol. 358, no. 6363, pp. 636–640, 2017.

[18] S. Klembt, T. H. Harder, O. A. Egorov, et al., "Exciton-polariton topological insulator," *Nature*, vol. 562, no. 7728, pp. 552–556, 2018.
[19] S. Malzard and H. Schomerus, "Nonlinear mode competition and symmetry-protected power oscillations in topological lasers," *New J. Phys.*, vol. 20, no. 6, p. 063044, 2018.
[20] G. Harari, M. A. Bandres, Y. Lumer, et al., "Topological insulator laser: Theory," *Science*, vol. 359, no. 6381, p. 1230, 2018.
[21] M. A. Bandres, S. Wittek, G. Harari, et al., "Topological insulator laser: Experiments," *Science*, vol. 359, no. 6381, p. 1231, 2018.
[22] M. Parto, S. Wittek, H. Hodaei, et al., "Edge-mode lasing in 1D topological active arrays," *Phys. Rev. Lett.*, vol. 120, no. 11, p. 113901, 2018.
[23] H. Zhao, P. Miao, M. H. Teimourpour, et al., "Topological hybrid silicon microlasers," *Nat. Commun.*, vol. 9, no. 1, pp. 1–6, 2018.
[24] Y. Ota, R. Katsumi, K. Watanabe, S. Iwamoto, and Y. Arakawa, "Topological photonic crystal nanocavity laser," *Commun. Phys.*, vol. 1, no. 1, pp. 1–8, 2018.
[25] Y. V. Kartashov and D. V. Skryabin, "Two-dimensional topological polariton laser," *Phys. Rev. Lett.*, vol. 122, no. 8, p. 083902, 2019.
[26] T. Ozawa, H. M. Price, A. Amo, et al., "Topological photonics," *Rev. Mod. Phys.*, vol. 91, no. 1, p. 015006, 2019.
[27] Y. Huang, W. Lou, F. Cheng, W. Yang, and K. Chang, "THz emission by frequency down-conversion in topological insulator quantum dots," *Phys. Rev. Appl.*, vol. 12, no. 3, p. 034003, 2019.
[28] K. Chang and W.-K. Lou, "Helical quantum states in HgTe quantum dots with inverted band structures," *Phys. Rev. Lett.*, vol. 106, no. 20, p. 206802, 2011.
[29] D. R. Candido, M. E. Flatté, and J. Carlos Egues, "Blurring the boundaries between topological and nontopological phenomena in dots," *Phys. Rev. Lett.*, vol. 121, p. 256804, 2018.
[30] A. Kundu, A. Zazunov, A. Levy Yeyati, T. Martin, and R. Egger, "Energy spectrum and broken spin-surface locking in topological insulator quantum dots," *Phys. Rev. B*, vol. 83, no. 12, p. 125429, 2011.
[31] S. Cho, D. Kim, P. Syers, N. P. Butch, J. Paglione, and M. S. Fuhrer, "Topological insulator quantum dot with tunable barriers," *Nano Lett.*, vol. 12, no. 1, pp. 469–472, 2012.
[32] Z. Wu, L. Lin, W. Yang, et al., "Spin-polarized charge trapping cell based on a topological insulator quantum dot," *RSC Adv.*, vol. 7, no. 49, pp. 30963–30969, 2017.
[33] S.-F. Zhang and W.-J. Gong, "Interference effect in the electronic transport of a topological insulator quantum dot," *J. Phys. Condens. Matter*, vol. 33, no. 13, p. 135301, 2021.
[34] M. A. Poyli, M. Hrtoň, I. A. Nechaev, et al., "Controlling surface charge and spin density oscillations by Dirac plasmon interaction in thin topological insulators," *Phys. Rev. B*, vol. 97, no. 11, p. 115420, 2018.
[35] M. S. Rider, S. J. Palmer, S. R. Pocock, X. Xiao, P. Arroyo Huidobro, and V. Giannini, "A perspective on topological nanophotonics: current status and future challenges," *J. Appl. Phys.*, vol. 125, no. 12, p. 120901, 2019.
[36] M. S. Rider, M. Sokolikova, S. M. Hanham, et al., "Experimental signature of a topological quantum dot," *Nanoscale*, vol. 12, no. 44, pp. 22817–22825, 2020.
[37] G. Siroki, D. K. K. Lee, P. D. Haynes, and V. Giannini, "Single-electron induced surface plasmons on a topological nanoparticle," *Nat. Commun.*, vol. 7, no. 1, pp. 1–6, 2016.
[38] L. Gioia, M. G. Christie, U. Zülicke, M. Governale, and A. J. Sneyd, "Spherical topological insulator nanoparticles: quantum size effects and optical transitions," *Phys. Rev. B*, vol. 100, no. 20, p. 205417, 2019.
[39] K.-I. Imura, Y. Yoshimura, Y. Takane, and T. Fukui, "Spherical topological insulator," *Phys. Rev. B*, vol. 86, no. 23, p. 235119, 2012.
[40] H. P. Paudel and M. N. Leuenberger, "Three-dimensional topological insulator quantum dot for optically controlled quantum memory and quantum computing," *Phys. Rev. B*, vol. 88, no. 8, p. 085316, 2013.
[41] L. A. Castro-Enriquez, L. F. Quezada, and A. Martín-Ruiz, "Optical response of a topological-insulator–quantum-dot hybrid interacting with a probe electric field," *Phys. Rev. A*, vol. 102, no. 1, p. 013720, 2020.
[42] G. D. Chatzidakis and V. Yannopapas, "Strong electromagnetic coupling in dimers of topological-insulator nanoparticles and quantum emitters," *Phys. Rev. B*, vol. 101, p. 165410, 2020.
[43] H. Peng, K. Lai, D. Kong, et al., "Aharonov–Bohm interference in topological insulator nanoribbons," *Nat. Mater.*, vol. 9, no. 3, pp. 225–229, 2010.
[44] D. Kong, J. C. Randel, H. Peng, et al., "Topological insulator nanowires and nanoribbons," *Nano Lett.*, vol. 10, no. 1, pp. 329–333, 2010.
[45] M. Tian, W. Ning, Z. Qu, H. Du, J. Wang, and Y. Zhang, "Dual evidence of surface Dirac states in thin cylindrical topological insulator Bi_2Te_3 nanowires," *Sci. Rep.*, vol. 3, no. 1, pp. 1–7, 2013.
[46] S. S. Hong, Y. Zhang, J. J. Cha, X.-L. Qi, and Y. Cui, "One-dimensional helical transport in topological insulator nanowire interferometers," *Nano Lett.*, vol. 14, no. 5, pp. 2815–2821, 2014.
[47] C.-W. Liu, Z. Wang, R. L. J. Qiu, and X. P. A. Gao, "Development of topological insulator and topological crystalline insulator nanostructures," *Nanotechnology*, vol. 31, no. 19, p. 192001, 2020.
[48] Y. Min, G. D. Moon, B. S. Kim, et al., "Quick, controlled synthesis of ultrathin bi2se3 nanodiscs and nanosheets," *J. Am. Chem. Soc.*, vol. 134, no. 6, pp. 2872–2875, 2012.
[49] H. Li, J. Cao, W. Zheng, et al., "Controlled synthesis of topological insulator nanoplate arrays on mica," *J. Am. Chem. Soc.*, vol. 134, no. 14, pp. 6132–6135, 2012.
[50] M. Veldhorst, C. G. Molenaar, X. L. Wang, H. Hilgenkamp, and B. Alexander, "Experimental realization of superconducting quantum interference devices with topological insulator junctions," *Appl. Phys. Lett.*, vol. 100, no. 7, p. 072602, 2012.
[51] A. Vargas, S. Basak, F. Liu, et al., "The changing colors of a quantum-confined topological insulator," *ACS Nano*, vol. 8, no. 2, pp. 1222–1230, 2014.
[52] X. Liu, J. Xu, Z. Fang, et al., "One-pot synthesis of Bi_2Se_3 nanostructures with rationally tunable morphologies," *Nano Res.*, vol. 8, no. 11, pp. 3612–3620, 2015.

[53] A. M. Dubrovkin, G. Adamo, J. Yin, et al., "Visible range plasmonic modes on topological insulator nanostructures," *Adv. Opt. Mater.*, vol. 5, no. 3, p. 1600768, 2017.
[54] C.-X. Liu, X.-L. Qi, H. J. Zhang, X. Dai, F. Zhong, and S.-C. Zhang, "Model Hamiltonian for topological insulators," *Phys. Rev. B*, vol. 82, no. 4, p. 045122, 2010.
[55] D. Bera, L. Qian, T.-K. Tseng, and P. H. Holloway, "Quantum dots and their multimodal applications: a review," *Materials*, vol. 3, no. 4, pp. 2260–2345, 2010.
[56] L. Jacak, P. Hawrylak, and A. Wojs, *Quantum Dots*, Berlin Heidelberg, Springer Science & Business Media, 2013.
[57] M. H. Kalos and P. A. Whitlock, *Monte Carlo Methods*, Weinheim, John Wiley & Sons, 2009.
[58] X. Zhu, L. Santos, R. Sankar, et al., "Interaction of phonons and Dirac fermions on the surface of Bi_2Se_3: a strong Kohn anomaly," *Phys. Rev. Lett.*, vol. 107, no. 18, p. 186102, 2011.
[59] X. Zhu, L. Santos, C. Howard, et al., "Electron-phonon coupling on the surface of the topological insulator Bi_2Se_3 determined from surface-phonon dispersion measurements," *Phys. Rev. Lett.*, vol. 108, no. 18, p. 185501, 2012.
[60] J. A. Sobota, S.-L. Yang, D. Leuenberger, et al., "Distinguishing bulk and surface electron-phonon coupling in the topological insulator Bi_2Se_3 using time-resolved photoemission spectroscopy," *Phys. Rev. Lett.*, vol. 113, no. 15, p. 157401, 2014.
[61] G. Martinez, B. A. Piot, M. Hakl, et al., "Determination of the energy band gap of Bi_2Se_3," *Sci. Rep.*, vol. 7, no. 1, pp. 1–5, 2017.

Supplementary Material: The online version of this article offers supplementary material (https://doi.org/10.1515/nanoph-2021-0292).